Biosensors and Bioelectronics 241 (2023) 115661

Contents lists available at ScienceDirect

Biosensors and Bioelectronics

journal homepage: www.elsevier.com/locate/bios

Multi-modal sensing with integrated machine learning to differentiate specific leukocytes targeted by electrically sensitive hybrid particles

Brandon K. Ashley [a], Jianye Sui [b], Mehdi Javanmard [a,b], Umer Hassan [a,b,c,*]

[a] Department of Biomedical Engineering, Rutgers, the State University of New Jersey, Piscataway, NJ, 08854, USA
[b] Department of Electrical and Computer Engineering, Rutgers, the State University of New Jersey, Piscataway, NJ, 08854, USA
[c] Global Health Institute, Rutgers, the State University of New Jersey, New Brunswick, NJ, 08901, USA

ARTICLE INFO

Keywords:
Biosensor
Microfluidics
Impedance cytometry
Biomarkers
Machine learning
Disease diagnostics

ABSTRACT

The growing need for personalized, accurate, and non-invasive diagnostic technology has resulted in significant advancements, from pushing current mechanistic limitations to innovative modality developments across various disease-related biomarkers. However, there still lacks clinical solutions for analyzing multiple biomarkers simultaneously, limiting prognosis for patients suffering with complicated diseases or comorbidities. Here, we conceived, fabricated, and validated a multifrequency impedance cytometry apparatus with novel frequency-sensitive barcoded metal oxide Janus particles (MOJPs) as cell-receptor targeting agents. These microparticles are modulated by a metal oxide semi-coating which exhibit electrical property changes in a multifrequency electric field and are functionalized to target CD11b and CD66b membrane proteins on neutrophils. A multi-modal system utilizing supervised machine learning and simultaneous high-speed video microscopy classifies immune-specific surface receptors targeted by MOJPs as they form neutrophil-MOJP conjugates, based on multivariate multifrequency electrical recordings. High precision and sensitivity were determined based on the type of MOJPs conjugated with cells (>90% accuracy between neutrophil-MOJP conjugates versus cells alone). Remarkably, the design could differentiate the number of MOJPs conjugated per cell within the same MOJP class (>80% accuracy); which also improved comparing electrical responses across different MOJP types (>75% accuracy) as well. Such trends were consistent in individual blood samples and comparing consolidated data across multiple samples, demonstrating design robustness. The configuration may further expand to include more MOJP types targeting critical biomarker receptors in one sample and increase the modality's multiplexing potential.

1. Introduction

Presently, several diseases are difficult to diagnose clinically due to lacking one highly correlated biomarker that can define its condition or state. This holds true for complicated, multifaceted diseases such as sepsis (Biron et al., 2015; Farooq and Colón-Franco, 2019; Hung et al., 2020; Kim and Choi, 2020), acute kidney injury (Oh, 2020; Wen and Parikh, 2021), many cancer types (Boissière-Michot et al., 2020; Ilie et al., 2012), and more (Khan et al., 2018; Patel and Sebastiani, 2020). For these conditions, a promising class of biomarkers may arise from immune cell surface receptors, which demonstrate rapid and highly correlated expression density responses from pathogen contact or inflammatory conditions (Schmidt et al., 2012; Sheneef et al., 2017; Weirich et al., 1998). Clinical research has pointed towards identifying these diseases through receptors such as CD64 (Hassan et al., 2017; Zeitoun et al., 2010), CD11b (Adib et al., 2007), C-type lectin (Chiffoleau, 2018; Tang et al., 2018), and CD66b (Schmidt et al., 2015) on myeloid-derived cells or CTLA-4 (Chang et al., 2013; Gao et al., 2015), CD18 (Abdel-Salam and Ebaid, 2014), and CD28 (Alegre et al., 2001; Petersen et al., 2019) on T cells. However, higher diagnostic accuracy in complicated diseases only comes from measuring a panel of these receptor biomarkers simultaneously. The bottleneck to collect this critical receptor data comes a shortage of relatively inexpensive techniques measuring multiple cell membrane proteins in one sample, explaining why many rapidly progressing diseases remain elusive to diagnose.

To measure many disease-related receptors quickly, a promising solution may come from point-of-care, multiplexing machines, which can analyze multiple biomarkers simultaneously using the same

* Corresponding author. Department of Biomedical Engineering, Rutgers, the State University of New Jersey, Piscataway, NJ, 08854, USA.
E-mail address: umer.hassan@rutgers.edu (U. Hassan).

https://doi.org/10.1016/j.bios.2023.115661
Received 5 June 2023; Received in revised form 29 August 2023; Accepted 31 August 2023
Available online 3 September 2023

investigative modality. Incorporating these targeting strategies on highly compartmentalized, point-of-care devices boasts several advantages including automated assay preparation (Lehmann et al., 2008; Sun et al., 2020; van de Groep et al., 2018) and integrated signal processing (Sun et al., 2014; Talukder et al., 2017). With these devices, diagnostics and disease outcomes may improve from smaller sample volumes required for miniaturized techniques (Ellett et al., 2018; Hassan et al., 2017), faster analysis (Uddin et al., 2016; Watkins et al., 2013), greater diagnostic accuracy by targeting multiple critical biomarkers (Cihalova et al., 2017; Lam et al., 2013), and increasing device availability across vast environmental and economical landscapes (Yeh et al., 2017; Zhang et al., 2020). From the multitude of point-of-care multiplexing techniques, impedance cytometry displays the highest potential for clinical translation. It can profile biological objects such as cells down to proteins and DNA nondestructively, and can provide fast electrical results (Ashley and Hassan, 2021a; Baraket et al., 2017; Petchakup et al., 2021; Saleh and Sohn, 2003). Additionally, fabrication upscaling makes it appealing for point-of-care settings (Hassan et al., 2017). However, presently its ability to discern multiple species simultaneously is limited without the use of detection parallelization or sensitive targeting agents, of which few options have been conceived.

For novel impedance-sensitive targeting agents with impedance cytometry, we recently reported a multiplexing modality using microparticles with varying metal oxide semi-coatings that are electrically identifiable using a multifrequency electric field (Xie et al., 2017). These barcoded metal-oxide Janus particles (MOJPs) can be differentiated both by metal oxide material, such as aluminum oxide, hafnium dioxide, and titanium dioxide, or layer thickness varying from 5 to 30 nm. Their mechanistic phenomenon arises from varying surface conductance across metal oxide thickness and materials, causing an impedance shift at distinct frequencies when subjected to an electric field. Furthermore, these MOJPs may be antibody-functionalized to target multiple cell-surface receptors at once (Ashley et al., 2022a,b), providing a solution for high-receptor multiplexing detection using a singular multifrequency excitation and detection source.

Herein, we present a multi-modal validation of MOJP detection when conjugated to neutrophils using multifrequency microfluidic impedance cytometry and simultaneous high-speed video microscopy. Fig. 1 represents impedance detection, which demonstrates functionalizing unique MOJPs to target CD11b and CD66b proteins on neutrophils using a streptavidin-biotin linker (Fig. 1B) (Ashley et al., 2021). When MOJPs conjugate to cells, unique electrical properties are recorded specific to the frequency-sensitive amplitude shifts detected by a tuned multifrequency electric field (Fig. 1E). High-speed video microscopy is used in synchronization with microfluidic impedance cytometry to confirm cell-MOJP conjugation. To achieve this, the Chronos 1.4 high speed camera was used, which can reach frame rates up to 35000 fps depending on resolution, along with internal storage up to 32 GB- which translates to approximately 16 s of real time storage per experiment. Additionally, the camera has functioned in similar applications for capturing microfluidic characteristics, making it an ideal choice to measuring cell and cell-MOJP conjugates under microfluidic flow (Chao et al., 2020; Duke et al., 2019; Ma et al., 2019; Wang et al., 2023). Conjugate identities were labeled both by MOJP type and the number of MOJPs conjugated per cell. Notably, supervised machine learning accomplished high-accuracy alignment of individual conjugate identities from electrical shifts alone, and differentiated across MOJP type, the number of MOJPs conjugated per cell, and across measured samples.

2. Materials and methods

2.1. Materials

The following was purchased from Sigma Aldrich (St. Louis, USA): phosphate buffered saline (PBS, 1X and 10X, pH = 7.2), Roswell Park Memorial Institute medium 1640 (RPMI), Ficoll-Paque density gradient, streptavidin, and (3-Amino-propyl) triethoxysilane (APTES). From Thermo Fisher Sceintific (Waltam, USA), biotinylated anti-CD11b monoclonal mouse antibody was purchased with greater than 95% sterility. From BioLegend (San Diego, USA), biotinylated anti-CD66b was purchased with greater than 98% sterility. From Southpoint Surgical Supply (Coral Springs, USA), a NE-300 syringe pump was purchased. Software used includes LabVIEW purchased and installed through National Instruments (Austin, USA) and MATLAB (v2020B) purchased and installed through MathWorks (Natick USA). The following was purchased from Zurich Instruments (Zurich, SUI): a

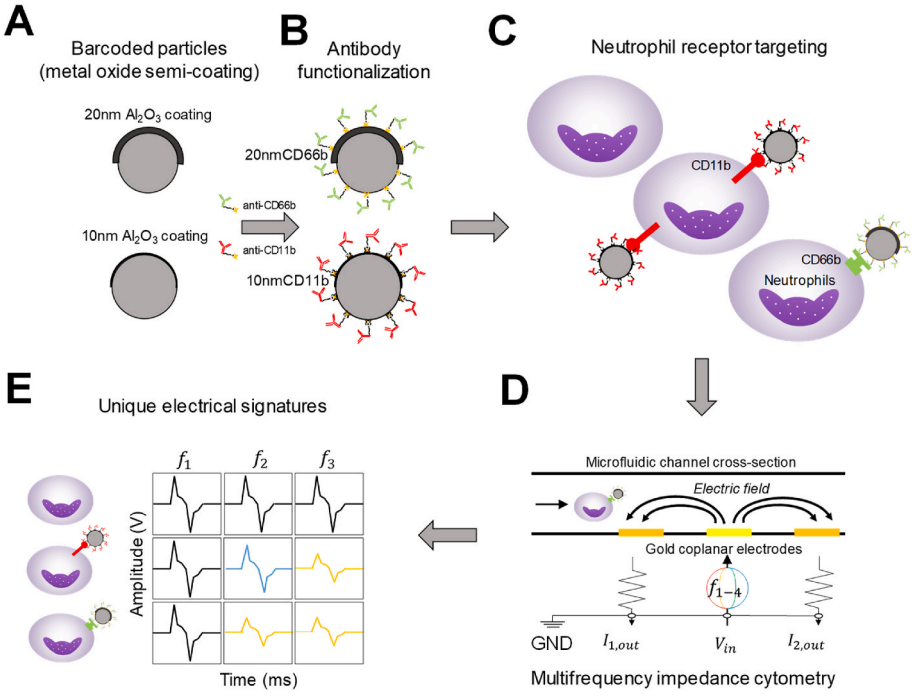

Fig. 1. Graphical overview of electrically-sensitive cell membrane receptor detection. (A) Polystyrene microparticles fabricated with different aluminum oxide-coatings (20 nm and 10 nm) are (B) functionalized with unique antibodies (anti-CD66b for 20 nm, anti-CD11b for 10 nm) to (C) target inflammatory-related neutrophil receptors forming cell-particle conjugates with receptor presence. (D) Objects are measured individually under flow using microfluidic impedance cytometry, with multiple frequencies applied that (E) isolate frequency responses unique to the aluminum oxide coated microparticle based on coating thickness.

HF2TA current amplifier and a HF2LI lock-in amplifier. A VWR Basic Inverted Microscope was purchased from VWR International (Radnor, USA). Through an institutional review board study, de-identified human blood was collected from Robert Wood Johnson Hospital (New Brunswick, USA). The Chronos 1.4 High Speed Camera was purchased from Kron Technologies (Vancouver, CAN).

2.2. Microfabrication of barcoded microparticles, microelectrodes, and microfluidic channels

Previous reports have extensively described manufacturing barcoded microparticles (Sui et al., 2020; Xie et al., 2017). The process briefly involves forming 3 μm polystyrene microparticles using nanosphere lithography. Then, 20 nm of gold is patterned on top of particles using electron-beam deposition. Finally, either 10 nm or 20 nm of aluminum oxide is patterned on top of the gold layer using atomic layer deposition, forming the aluminum oxide-coated Janus microparticles (MOJP).

Additionally, the procedures of fabricating gold microelectrodes and microfluidic channels are described in previous publications (Ashley and Hassan, 2021b). To summarize, photoresist-covered borosilicate wafers are treated with UV light through a photomask with electrode geometries, and chromium (250 nm) and gold (750 nm) were deposited above (Fig. 2Ai). Similarly, the microchannel structure is rendered on top of silicon wafers after UV exposure using photolithography. PDMS cures over the microchannel pillars after APTES wafer treatment and is removed with the channel dimensions. Following O_2 plasma exposure, the channel and electrodes are bonded, with channel focusing regions positioned between electrodes (Fig. 2Aii). Finally, the device is adhered to a microscope stage using tape and connects with a lock-in amplifier and current amplifying circuit using silver conductive epoxy (Fig. 2Aiv).

2.3. Barcoded microparticle functionalization

Functionalizing barcoded microparticles with receptor-targeting antibodies has also been defined in previous reports (Ashley et al., 2021, 2022). In short, 2 μL of SAv (0.1 mg/mL) is mixed with either 200 μL of 20 nm MOJPs (SAv/20 nm) or 10 nm MOJPs (SAv/10 nm), each at a particle concentration of $6.0x10^7$ particles/mL. These mixtures are then centrifuged and washed to eliminate unbound SAv. After SAv adsorption to MOJPs, antibody functionalization is achieved after combining 10 μL of biotinylated anti-CD66b antibody (1 mg/mL in 1X PBS) with the SAv/20 nm solution (20nmCD66b) and 10 μL of biotinylated anti-CD11b antibody (1 mg/mL in 1X PBS) is combined to the SAv/10 nm solution (10nmCD11b).

2.4. Neutrophil isolation and microparticle conjugation

To isolate neutrophils, blood samples from de-identified patients were obtained from Robert Wood Johnson University Hospital. Once collected, blood was mixed with 1X PBS at 1:1 ratio, and that mixture was combined with Ficoll-Paque density gradient at a 2:3 ratio. After centrifugation of the solution to remove plasma, platelets, and red blood cells, non-neutrophil mononuclear cells were lysed and aspirated by adding short durations of deionized water followed by tonicity leveling using 10X PBS. Non-neutrophil mononuclear cell lysing steps were repeated until a gray neutrophil pellet arose, which was then constituted in RPMI 1640 media at a 1:10 ratio (Wagner et al., 2021).

After isolated neutrophil preparation, either 10nmCD11b particle or 20nmCD66b particle solutions were mixed with diluted neutrophils at a 10:1 particle-cell ratio and incubated for 1 h. Samples measured without MOJPs (cells alone) consisted of neutrophils diluted in 1X PBS were also incubated for 1 h.

2.5. Multifrequency impedance cytometer interfacing, signal acquisition, and signal processing

In the microelectrode configuration, the center electrode carries a 10V input with various input frequencies of 500 kHz, 7.5 MHz, 8.3 MHz, and 9 MHz, while the exterior electrodes are grounded in series with 10kΩ resistors. A LabVIEW custom script acquires the signal, which involves current-to-voltage recording conversion and transimpedance multiplication. Following this, a differential amplifier subtracts the inputs from the two grounded electrodes and is sampled at 250 kHz. The four frequencies are then demodulated and isolated into distinct arrays using a lock-in amplifier. Digital filters using MATLAB are applied for signal normalization which mitigates background noise and consists of a 20 Hz 4^{th} order high-pass Butterworth filter, a 100 Hz 4^{th} order low-pass Butterworth filter, and 1^{st} order band-stop Butterworth filters at 60 Hz and 120 Hz. Electrical recordings are produced for each of the selected four frequencies. For neutrophil or neutrophil-particle conjugate counting, a voltage bipolar amplitude 15 times greater than the noise standard deviation indicates their presence.

2.6. Multi-modal high-speed video microscopy

A C-mount attaches the Chronos 1.4 high-speed camera to the inverted microscope's eyepiece, set to a 1280x360 resolution ratio, 4500 recording frames per second, and a shutter rate of 25 μs. Along with camera specifications, a virtual Ethernet interface via micro-USB connection along with the manufactures support for a network IP with the camera over a local internet connection allows for remote camera access. The camera was accessed by a LabVIEW script control for starting and stopping recordings simultaneous to electrical recordings, ensuring data synchronization. Cell-particle conjugation and counting the number of particles attached was performed with manual visual inspection of images occurring at the exact time electrical pulses were recorded.

A custom MATLAB program identifies an electrical pulse threshold to isolate neutrophil pulses from residual red blood cells (RBCs) and unconjugated MOJPs pulses. When neutrophil pulses are identified, the MATLAB script extracts video frames corresponding to the triggered electrical time point and is manually assigned to different arrays based on visualized cell-MOJP conjugation and, if so, how many particles are attached at once. The program then stores bipolar pulse amplitude and pulse width data from each demodulated frequency for 4 frequency data inputs in each classified array group.

2.7. Machine learning

Using MATLAB's Classification Learner application, supervised machine learning was implemented and training, validation, and testing across a myriad of support vector machines (SVM) neural network (NN) models were performed. High-speed video microscopy images assign neutrophil or neutrophil-MOJP conjugate identities, and the bipolar amplitudes for each pulse across the four demodulated frequencies are the 4 features assigned to each data point. Two-group comparisons are assessed, with 80% of selected data for model training and 20% for testing. Accuracy, data counts, and receiver operating characteristic curves (ROC) are reported from the highest testing accuracy models (SI Fig. 1). For the SVM models, all of them used 1 as a box constraint value. For the NN models, a rectified linear unit activation function was used, the iteration limit was capped to 1000, and a 0.01 learning rate was used. Both SVM and NN models performed data standardization before training and testing, and the number of data points across groups were not selectively balanced owing to varying cellular concentrations in each blood sample. Further SVM, and NN model parameters (SI Table 1) and performance metric information is provided in the Supplemental Information.

3. Results and discussion

3.1. Multi-modal data collection and pulse amplitude representation

Fig. 2 shows the representative electrical pulse data and corresponding images extracted from the saved high-speed video recordings with the multifrequency microfluidic impedance cytometer. As pointed out in Fig. 2B with the overlaid pulses for each frequency, neutrophil pulse amplitudes are higher compared to other sample objects, making it ideal to use amplitude thresholding to isolate from competing analytes such as residual red blood cells (RBCs) and unconjugated MOJPs. With the selected camera conditions, images have low but discernible light exposure while producing sharp frame-to-frame object clarity (Fig. 2C), which is most important when object identities are determined from image frames in the video recording. Fig. 2C details different cell identities, such as individual neutrophils alone (Fig. 2Ci) shown with blue arrows compared to neutrophils with different MOJPs attached at different positions (Fig. 2Cii and Fig. 2Ciii), highlighted with red arrows. The corresponding expanded electrical pulse data for each of these objects is shown by Fig. 2D.

After this manual classification, the changes in bipolar pulse amplitudes related to each object are assigned and compared. SI Fig. 2 displays the bulk amplitude data for each collected object across all conducted experiments with this design. As stated earlier, the number of particles attached per cell were separated into different groups to evaluate the sensitivity in electrically differentiating cell-particle conjugation based on this, since it is expected that more MOJPs conjugated per cell will multiply its frequency-sensitive amplitude shifts. It is also expected that 20 nm MOJPs will experience its lower pulse amplitude shift at a lower frequency compared to the 10 nm MOJPs (Sui et al., 2020). While loosely correlated, this is affirmed from a slightly lower amplitude slope for cell-20nmCD66b amplitudes at the 7.5 MHz frequency versus the cell-10nmCD11b amplitudes, which is no longer apparent in at the 8.3 MHz frequency, and the average amplitude is lower for cell-10nmCD11b pulses at 9 MHz versus the cell-20nmCD66b data (SI Fig. 2).

When dividing by the MOJP type and the number of those particles attached to cells, six different groups are categorized; seven when including cells without any particles attached. There appears to be large amplitude changes across the frequency spectra when normalized to an objects 500 kHz amplitude (SI Fig. 2D). The first evident observation is much larger normalized amplitudes for cells without any particles attached, which may factor into its high differentiation determined from the machine learning results. The lower 7.5 MHz amplitude is evident with Cells-20nmCD66b conjugate groups, but it is also shown that the number of MOJPs attached does indeed multiple their frequency effects, with the relative bulk frequency reductions occurring for both 10nmCD11b and 20nmCD66b particles as the number of particles conjugated increases. There also appears to be more similarity in normalized amplitude for the same number of particles conjugated across MOJP types (i.e., Cells-[1] 10nmCD11b versus Cells-[1] 20nmCD11b), although their polarization shifts towards their specific closest frequency is lower than the corresponding amplitude of the other (7.5 MHz is lower for Cells-[1] 20nmCD66b, 8.3 MHz is lower for Cells-[1] 10nmCD11b). This relationship is similar but does not hold completely accurate as the number of particles conjugated increases across samples, which may point towards the dynamic nature of MOJPs. Depending on if the MOJPs are conjugated at a position where they are in contact, this may alter their frequency impedance shift and likewise their amplitude magnitude with the frequencies used in these experiments.

3.2. Machine learning comparing cell-conjugate variants within individual samples

Machine learning was then used on the more specific cell-MOJP conjugate groups to better determine where signal changes were originating. Here, comparisons are shown as the average accuracy across measured neutrophil samples (n=3) by Fig. 3 and SI Table 2. Fig. 3A dissects the accuracy in separating different numbers of particles attached relative to cells with no particles attached. At this point, there was higher differentiation as the number of particles conjugated increased for both groups, which points towards the compounding effect the number of particles has on the signal amplitude at specific frequencies. This only affirms where the high signal separation comes from when knowing if particles are attached, but it also important to find differences within the same particle types as this may quantify a degree of expression density on cells that could translate to clinical significance.

Fig. 3B specifies the accuracy in separating groups within the same particle class by the number of particles conjugated to a given cell. Here, the largest differences come from particle numbers that are non-consecutive (i.e., 1 particle versus 3 or more particles attached), where the degrees of separation between consecutive number of particles conjugated is lower but still all above 80% accuracy. While previously not considered to separate the number of particles attached, this may point towards a promising system sensitivity in identifying receptor expression density, where a proportional relationship would exist between cell-receptor expression and number of conjugated MOJPs.

The ability to differentiate signals by the different type of MOJP conjugated demonstrates this architectures' multiplexing potential and clinical significance. Dividing groups by the number of particles attached can help separate signal data across the type of MOJPs as well. Fig. 3C shows those comparisons, with each number of particles attached to cells being compared across MOJP type. Again, higher comparisons are seen across cohorts with greater differences in the number of particles attached, while the same number of particles attached had the lowest accuracy (Fig. 3C gray bar plots). Further limitations may also come from the small amplitude shifts MOJPs provide at different frequencies relative to neutrophil pulse dominance, hindering the sensitivity to differentiate them across MOJP types. Nonetheless, nearly all comparisons had accuracies higher versus only considering all number of particles conjugated to cells between the MOJP types (Fig. 3C purple bar plot) and were better confirmed by larger changes in the pulse amplitude data at more representative applied frequencies. SI Table 2 also summarizes the reported average accuracy, area under the ROC curve (AUC ROC), sensitivity, and specificity across different samples. Finally, information on individual sample comparisons is provided in the supplemental information (SI Figs. 3–5, SI Tables 3–5), which follows average trends closely labeling cells alone and cells with individual MOJPs conjugated.

3.3. Evaluating pooled sample data for inter-sample, repeatable accuracy

After evaluating the average machine learning outcomes from individual samples measured, the entire data across samples were combined to assess the impacts of sample and device variability on the sensitivity of electrically determining cell-MOJP conjugate groups. Fig. 4 and SI Table 6 showcases a similar methodology to the previous section but single comparisons using the pooled data across samples to form individual machine learning evaluations. Firstly, cells alone versus any cell-MOJP iteration yields greater than 80% accuracy (Fig. 4A), which points towards the ability to measure MOJP presence on a binary level and can function as an individual biomarker detection mode. Expanding on MOJP presence, Fig. 4B also holds similar accuracy trends comparing the number of MOJPs conjugated per cell when making calculations within the same MOJP class. Here, greater than 85% accuracy was reported, and this defines the impedance detection sensitivity within the same MOJP and likewise receptor expression density the MOJP targets. Fig. 4C then disseminates the design's multiplexing sensitivity by reporting machine learning accuracies across MOJP types. While the bulk comparison without considering the number of conjugated MOJPs per cell had relatively low accuracy at 71.3% (Fig. 4C purple bar plot),

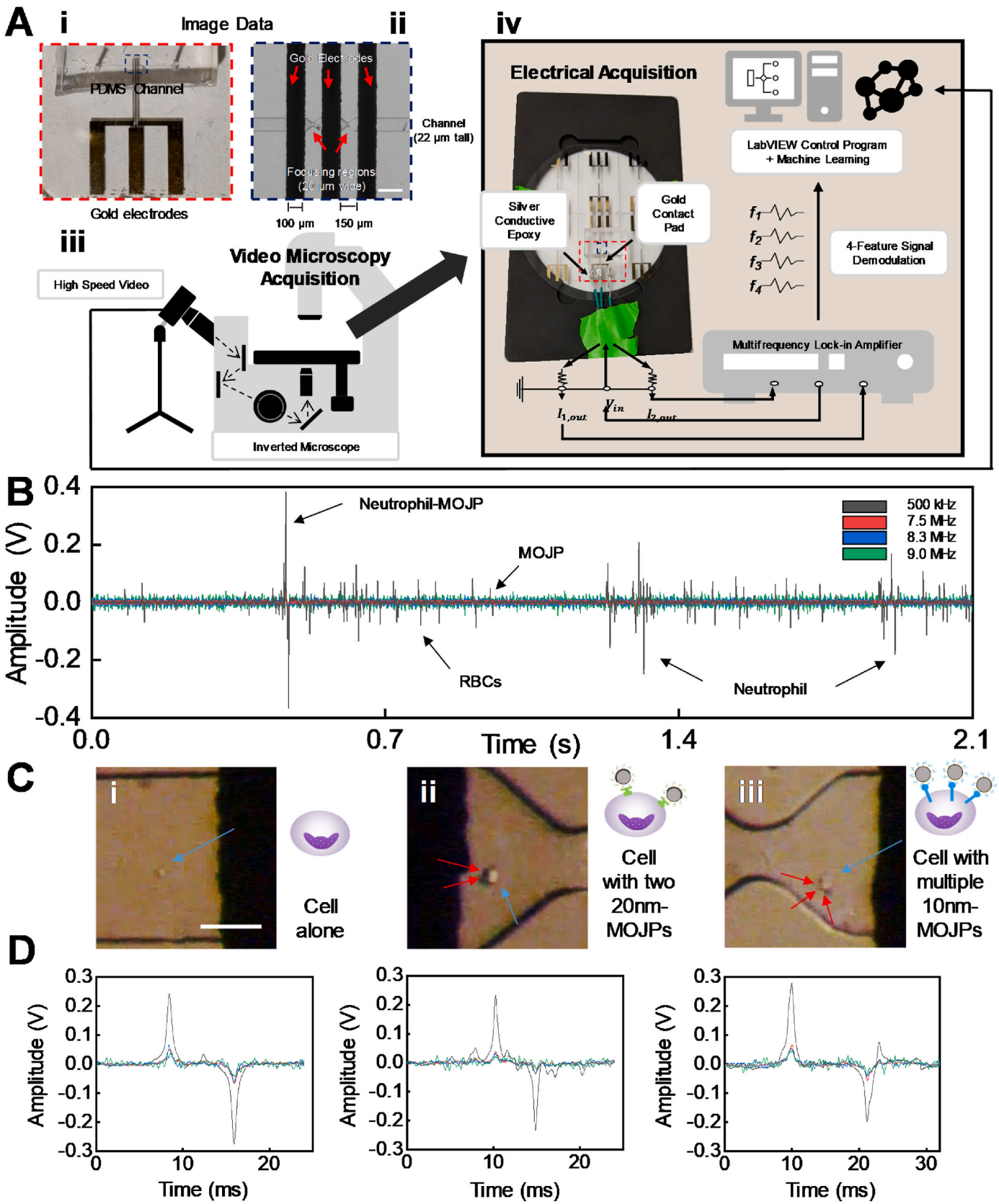

Fig. 2. Multifrequency impedance cytometer and high-speed video microscopy instrumentation and data collection overview. (A) Gold microelectrodes with polydimethylsiloxane (PDMS)-based microfluidic channels are staged above an inverted microscope with a mounted high-speed video camera for simultaneous electrical-video recording. Electrodes are bonded with current amplifying circuitry, with data management and processing controlled via LabVIEW and machine learning utilized for multi-variate differentiation. (B) Blood cells and metal oxide-coated Janus microparticle (MOJP) electrical responses over four recorded voltage frequencies at 500 kHz (gray), 7.5 MHz (red), 8.3 MHz (blue), and 9 MHz (green). (C) Microscope images (scale bar = 35 μm) captured from high-speed camera video recordings for neutrophils (blue arrows) without or with conjugated MOJPs (red arrows) and (D) their corresponding species bipolar pulse amplitudes.

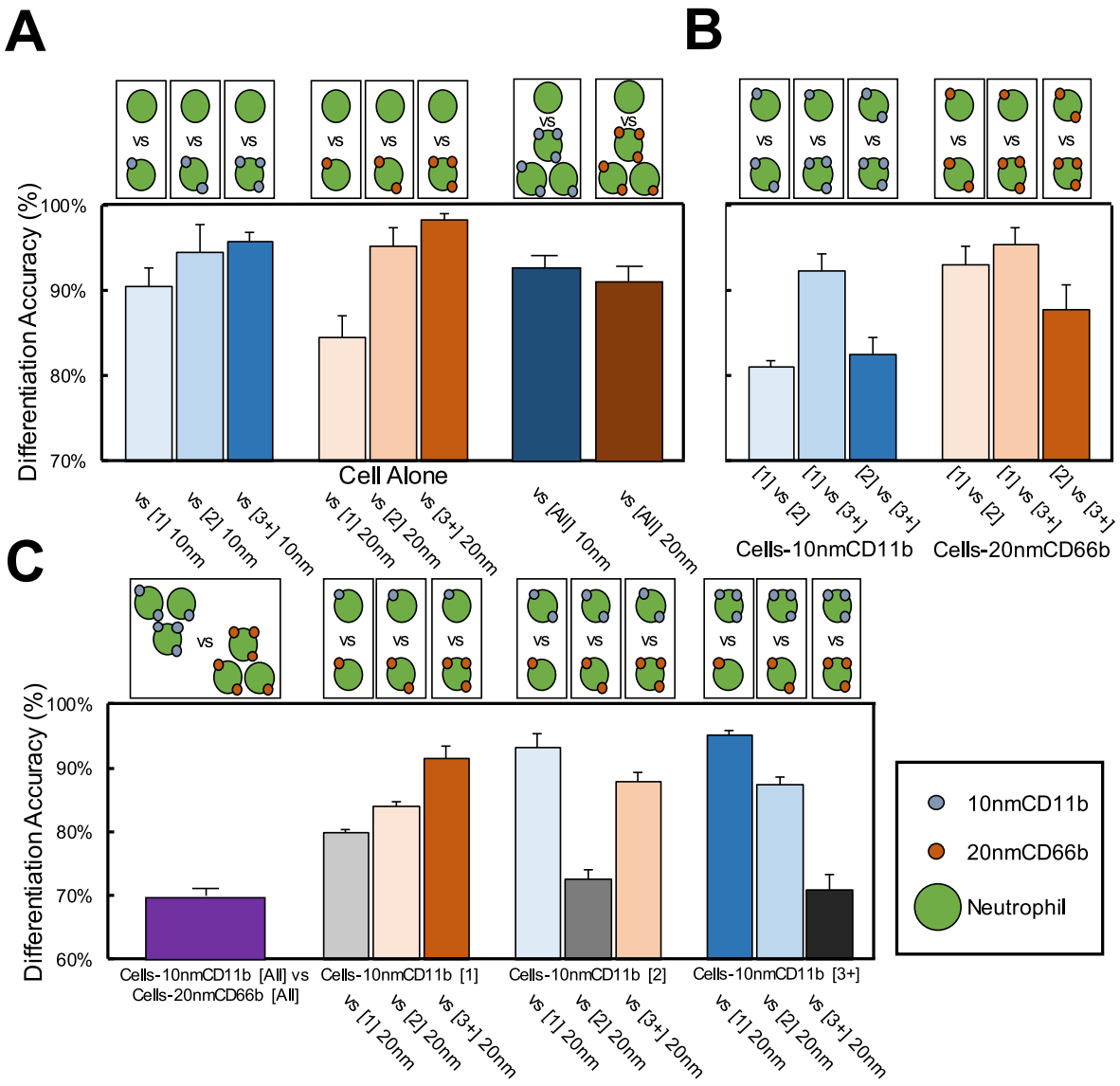

Fig. 3. Average reported accuracy differentiating different classified groups using their multifrequency electrical data and machine learning (n=3 samples). (A) Reported receptor presence: accuracy differentiating cells alone versus different cell-particle conjugate configurations by particle type and number of particles conjugated. (B) Reported electrical sensitivity: accuracy comparing ability to differentiate cell-particle conjugates by the number of conjugated particles within the same particle type. (C) Reported multiplexing potential: accuracy differentiating cell-particle conjugates across particle types. Error bars = standard error of the mean (S.E.M.).

expanding to consider the number of conjugated MOJPs per cell then produced higher accuracies by pinpointing multiplied amplitude effects with increasing number of conjugated particles along with the frequency-dependent amplitude shifts across MOJP type.

Beyond accuracy, Fig. 4D plots ROC curves for each of the comparisons from the pooled cell-MOJP conjugate data, with separate plots to group results similar to the accuracy bar plots from Fig. 4A–C. While accuracy is a significant metric for a models function, the ROC curves and area under the ROC curves (AUC ROC) are a more discriminate paradigm which is more robust against unequal data size comparisons and overall a better clinical diagnostic evaluator (Ashley et al., 2022a, b). Given this, trends with accuracy and AUC ROC hold consistent with the pooled data, as all AUC ROCs are over 75% while many are over 95% (total plot area = 100%). Likewise, models with high accuracy exhibited high AUC ROCs (Cells alone vs Cells-[3+] 10nmCD11b, Cells-[3+] 10nmCD11b vs Cells-[1] 20nmCD66b), while the lowest accuracy comparisons also had the lowest AUC ROCs (Cells-[All] 10nmCD11b vs Cells-[All] 20nmCD66b, Cells-[3+] 10nmCD11b vs Cells-[3+] 20nmCD66b).

With the pooled data having high model accuracies and AUC ROCs, this demonstrates the electrical variability introduced between different sample impedance or baseline measurements from different impedance cytometers are insignificant compared to the frequency-sensitive amplitude effects resulting from MOJPs conjugated to cells. It also shows that the machine learning models recognize these changes from the unique barcoded amplitude changes from the four applied frequencies and this unique response is robust compared to external noise contributors and inter-experimental variances. Overall, there are insignificant sensitivity differences electrically identifying 10nmCD11b MOJPs versus 20nmCD66b MOJPs using this system, as similar accuracies and AUC ROCs were reported independent of the MOJP type. Future studies are in progress to confirm these electrical signature trends between conjugates in the same sample and how object electrical identity may change if more than one MOJP type is conjugated to the same cell.

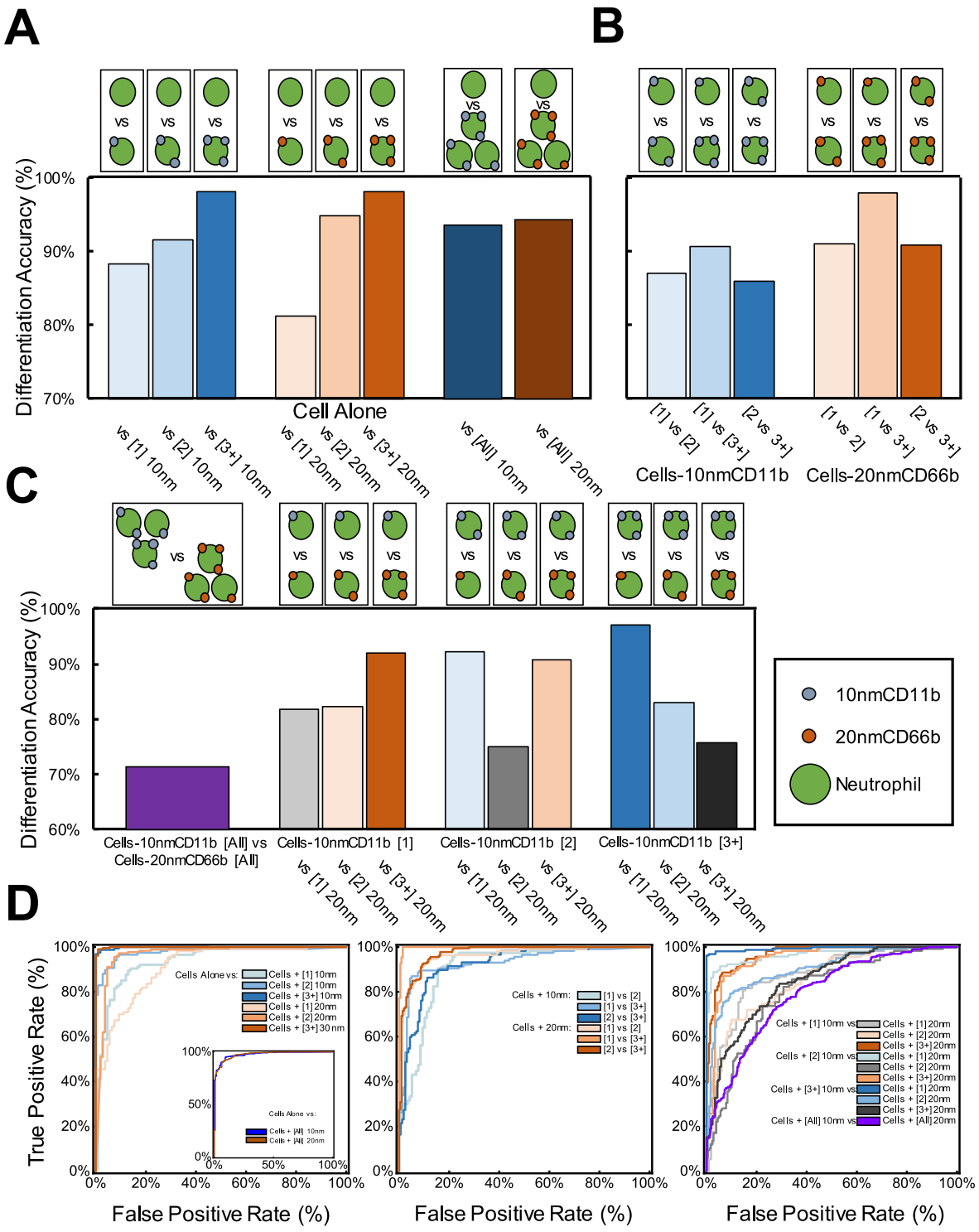

Fig. 4. Reported accuracy differentiating different classified groups using their multifrequency electrical data and machine learning when pooling data across all collected samples. (A) Reported receptor presence: accuracy differentiating cells alone versus different cell-particle conjugate configurations by particle type and number of particles conjugated. (B) Reported electrical sensitivity: accuracy comparing ability to differentiate cell-particle conjugates by the number of conjugated particles within the same particle type. (C) Reported multiplexing potential: accuracy differentiating cell-particle conjugates across particle types. (D) Receiver operating characteristic curves of pooled data for the 24 unique group comparisons performed.

4. Conclusion

Electrically sensitive barcoded microparticles were measured with multifrequency impedance cytometry, with simultaneous high-speed video microscopy that enabled supervised machine learning to identify cell-particle configurations using their multi-parameter frequency responses. Here, a high accuracy was found comparing 10nmCD11b-cell and 20nmCD66b-cell conjugates to cells alone (both >90%). While bulk comparisons of 10nmCD11b-cell and 20nmCD66b-cell conjugates were lower (69.8% accuracy), the expansion of electrical signatures to the number of particles attached within MOJP types increased accuracy in identifying objects electrically (up to 98% accuracy). This demonstrated

the ability to characterize receptor expression density as the number of particles per cell could also be counted. High accuracy was maintained both with replicate experiments and after pooling all sample data together. To determine the efficacy using MOJP as cell receptor profiling tools, more MOJP types should be characterized in future studies (i.e., hafnium dioxide-coated, titanium dioxide-coated), along with using separate-sample machine learning models to validate 10nmCD11b and 20nmCD66b particles combined in the same sample for assessing the modality's true multiplexing potential. There will also be future characterizations into MOJP conjugation rates with known receptor expression using parallel receptor control experiments with an emphasis on understanding a patient's receptor expression profile.

CRediT authorship contribution statement

Brandon K. Ashley: Methodology, Data curation, Formal analysis, Funding acquisition, Visualization, Writing – original draft, Writing – review & editing. **Jianye Sui:** Methodology. **Mehdi Javanmard:** Conceptualization, Supervision, Funding acquisition, Writing – review & editing. **Umer Hassan:** Conceptualization, Funding acquisition, Supervision, Methodology, Project administration, Resources, Writing – review & editing.

Declaration of competing interest

The authors declare the following financial interests/personal relationships which may be considered as potential competing interests: Umer Hassan reports financial support was provided by National Science Foundation. Umer Hassan and Mehdi Javanmard reports a relationship with National Science Foundation that includes: funding grants.

Data availability

Data will be made available on request.

Acknowledgements

Authors would like to thank Dr. Jonathan McCoy for help in IRB process and Muhammad Nabeel Tahir for his contributions with the data analysis. Authors acknowledge support from the National Science Foundation (NSF) Award Number 200251, National Institute of General Medical Sciences (NIGMS) as part of the National Institute of Health's (NIH) training grant T32 GM135141, Rutgers VCRI-Busch Biomedical Research grant, and Rutgers School of Graduate Studies and School of Engineering.

Appendix A. Supplementary data

Supplementary data to this article can be found online at https://doi.org/10.1016/j.bios.2023.115661.

References

Abdel-Salam, B.K.A., Ebaid, H., 2014. Cent.-Eur. J. Immunol. 39, 209–215. https://doi.org/10.5114/ceji.2014.43725.
Adib, M., Ostadi, V., Navaei, F., Fosoul, F.S., Oreizi, F., Shokouhi, R., Bakhshiani, Z., 2007. Iran. J. Allergy Asthma Immunol. 93–96.
Alegre, M.-L., Frauwirth, K.A., Thompson, C.B., 2001. 1, 220–228 https://doi.org/10.1038/35105024.
Ashley, B.K., Hassan, U., 2021a. WIREs Nanomedicine Nanobiotechnology 13, e1701. https://doi.org/10.1002/wnan.1701.
Ashley, B.K., Hassan, U., 2021b. Biotechnol. Bioeng. 118, 4428–4440. https://doi.org/10.1002/bit.27910.
Ashley, B.K., Sui, J., Javanmard, M., Hassan, U., 2022a. Lab Chip 22, 3055–3066. https://doi.org/10.1039/D2LC00563H.
Ashley, B.K., Sui, J., Javanmard, M., Hassan, U., 2022b. In: IEEE 17th International Conference on Nano/Micro Engineered and Molecular Systems (NEMS). Presented at the 2022 IEEE 17th International Conference on Nano/Micro Engineered and Molecular Systems (NEMS), pp. 211–216. https://doi.org/10.1109/NEMS54180.2022.9791160.
Ashley, B.K., Sui, J., Javanmard, M., Hassan, U., 2021. Anal. Bioanal. Chem. 413, 555–564. https://doi.org/10.1007/s00216-020-03026-4.
Baraket, A., Lee, M., Zine, N., Sigaud, M., Bausells, J., Errachid, A., 2017. Biosens. Bioelectron., special issue selected papers from the 26th anniversary world congress. Biosensors 93, 170–175. https://doi.org/10.1016/j.bios.2016.09.023.
Biron, B.M., Ayala, A., Lomas-Neira, J.L., 2015. Biomark. Insights 10s4. https://doi.org/10.4137/BMI.S29519. BMI.S29519.
Boissière-Michot, F., Jacot, W., Fraisse, J., Gourgou, S., Timaxian, C., Lazennec, G., 2020. Cancers 12, 2076. https://doi.org/10.3390/cancers12082076.
Chang, K.C., Burnham, C.-A., Compton, S.M., Rasche, D.P., Mazuski, R., SMcDonough, J., Unsinger, J., Korman, A.J., Green, J.M., Hotchkiss, R.S., 2013. Crit. Care 17, R85. https://doi.org/10.1186/cc12711.
Chao, C., Jin, X., Fan, X., 2020. Langmuir 36, 15102–15111.
Chiffoleau, E., 2018. Immunol, vol. 9. https://doi.org/10.3389/fimmu.2018.00227.
Cihalova, K., Hegerova, D., Jimenez, A.M., Milosavljevic, V., Kudr, J., Skalickova, S., Hynek, D., Kopel, P., Vaculovicova, M., Adam, V., 2017. J. Pharm. Biomed. Anal. 134, 325–332. https://doi.org/10.1016/j.jpba.2016.10.025.
Duke, D.J., Knast, T., Thethy, B., Gisler, L., Edgington-Mitchell, D., 2019. Meas. Sci. Technol. 30, 075403 https://doi.org/10.1088/1361-6501/ab1832.
Ellett, F., Jorgensen, J., Marand, A.L., Liu, Y.M., Martinez, M.M., Sein, V., Butler, K.L., Lee, J., Irimia, D., 2018. Nat. Biomed. Eng. 2, 207–214. https://doi.org/10.1038/s41551-018-0208-z.
Farooq, A., Colón-Franco, J.M., 2019. J. Appl. Lab. Med. 3, 716–719. https://doi.org/10.1373/jalm.2017.025916.
Gao, D.-N., Yang, Z.-X., Qi, Q.-H., 2015. Int. J. Clin. Exp. Med. 8, 18998–19005.
Hassan, U., Ghonge, T., R Jr., B., Patel, M., Rappleye, M., Taneja, I., Tanna, A., Healey, R., Manusry, N., Price, Z., Jensen, T., Berger, J., Hasnain, A., Flaugher, E., Liu, S., Davis, B., Kumar, J., White, K., Bashir, R., 2017. Nat. Commun. 8, 15949 https://doi.org/10.1038/ncomms15949.
Hung, S.-K., Lan, H.-M., Han, S.-T., Wu, C.-C., Chen, K.-F., 2020. Biomedicines 8, 494. https://doi.org/10.3390/biomedicines8110494.
Ilie, M., Hofman, V., Ortholan, C., Bonnetaud, C., Coëlle, C., Mouroux, J., Hofman, P., 2012. Cancer 118, pp. 1726–1737. https://doi.org/10.1002/cncr.26456.
Khan, S.Q., Khan, I., Gupta, V., 2018. 5, 52 https://doi.org/10.3389/fmed.2018.00052.
Kim, M.H., Choi, J.H., 2020. Infect. Chemother. 52, 1–18. https://doi.org/10.3947/ic.2020.52.1.1.
Lam, B., Das, J., Holmes, R.D., Live, L., Sage, A., Sargent, E.H., Kelley, S.O., 2013. Nat. Commun. 4 https://doi.org/10.1038/ncomms3001, 2001.
Lehmann, L.E., Hunfeld, K.-P., Emrich, T., Haberhausen, G., Wissing, H., Hoeft, A., Stüber, F., 2008. Med. Microbiol. Immunol. 197, 313–324. https://doi.org/10.1007/s00430-007-0063-0.
Ma, T., Sun, S., Li, B., Chu, J., 2019. Actuators Phys 292, 90–96. https://doi.org/10.1016/j.sna.2019.04.005.
Oh, D.-J., 2020. Ren. Fail. 42, 154–165. https://doi.org/10.1080/0886022X.2020.1721300.
Patel, K., Sebastiani, G., 2020. JHEP Rep 2, 100067. https://doi.org/10.1016/j.jhepr.2020.100067.
Petchakup, C., Hutchinson, P.E., Tay, H.M., Leong, S.Y., Li, K.H.H., Hou, H.W., 2021. Sensor. Actuator. B Chem. 339, 129864 https://doi.org/10.1016/j.snb.2021.129864.
Petersen, L.E., Schuch, J.B., de Azeredo, L.A., Baptista, T.S.A., Motta, J.G., do Prado, A. D., Bauer, M.E., 2019. Clin. Rheumatol. 38, 2909–2915. https://doi.org/10.1007/s10067-019-04615-0.
Saleh, O.A., Sohn, L.L., 2003. Proc. Natl. Acad. Sci. U.S.A. 100, 820–824. https://doi.org/10.1073/pnas.0337563100.
Schmidt, T., Brodesser, A., Schnitzler, N., Grüger, T., Brandenburg, K., Zinserling, J., Zündorf, J., 2015. PLoS One 10, e0132703. https://doi.org/10.1371/journal.pone.0132703.
Schmidt, T., Zündorf, J., Grüger, T., Brandenburg, K., Reiners, A.-L., Zinserling, J., Schnitzler, N., 2012. J. Leukoc. Biol. 91, 791–802. https://doi.org/10.1189/jlb.0911483.
Sheneef, A., Mohamed, T., Boraey, N.F., Ashry, M., 2017. Egypt. J. Immunol. 24, 29–36.
Sui, J., Xie, P., Lin, Z., Javanmard, M., 2020. Talanta 215, 120791. https://doi.org/10.1016/j.talanta.2020.120791.
Sun, A., Wambach, T., Venkatesh, A.G., Hall, D.A., 2014. In: IEEE Biomedical Circuits and Systems Conference (BioCAS) Proceedings. Presented at the 2014 IEEE Biomedical Circuits and Systems Conference (BioCAS) Proceedings, pp. 312–315. https://doi.org/10.1109/BioCAS.2014.6981725.
Sun, L.L., Leo, Y.S., Zhou, X., Ng, W., Wong, T.I., Deng, J., 2020. Mater. Sci. Energy Technol. 3, 274–281. https://doi.org/10.1016/j.mset.2019.10.007.
Talukder, N., Furniturewalla, A., Le, T., Chan, M., Hirday, S., Cao, X., Xie, P., Lin, Z., Gholizadeh, A., Orbine, S., Javanmard, M., 2017. Biomed. Microdevices 19, 36. https://doi.org/10.1007/s10544-017-0161-8.
Tang, J., Lin, G., Langdon, W.Y., Tao, L., Zhang, J., 2018. Front. Immunol. 9 https://doi.org/10.3389/fimmu.2018.00123.
Uddin, R., Burger, R., Donolato, M., Fock, J., Creagh, M., Hansen, M.F., Boisen, A., 2016. Biosens. Bioelectron. 85, 351–357. https://doi.org/10.1016/j.bios.2016.05.023.
van de Groep, K., Bos, M.P., Savelkoul, P.H.M., Rubenjan, A., Gazenbeek, C., Melchers, W.J.G., van der Poll, T., Juffermans, N.P., Ong, D.S.Y., Bonten, M.J.M., Cremer, O.L., 2018. On behalf of the MARS consortium. Eur. J. Clin. Microbiol. Infect. Dis. 37, 1333–1344. https://doi.org/10.1007/s10096-018-3255-1.
Wagner, K., Sami, M.A., Norton, C., McCoy, J., Hassan, U., 2021. RSC Adv. 11, 21315–21322. https://doi.org/10.1039/D1RA02759J.
Wang, X., Wang, Y., Yang, X., Li, B., Chu, J., 2023. IEEE Trans. Biomed. Eng. 70, 573–580. https://doi.org/10.1109/TBME.2022.3197649.

Watkins, N.N., Hassan, U., Damhorst, G., Ni, H., Vaid, A., Rodriguez, W., Bashir, R., 2013. Sci. Transl. Med. 5 https://doi.org/10.1126/scitranslmed.3006870, 214ra170-214ra170.

Weirich, E., Rabin, R.L., Maldonado, Y., Benitz, W., Modler, S., Herzenberg, Leonard A., Herzenberg, Leonore A., 1998. J. Pediatr. 132, 445–451. https://doi.org/10.1016/S0022-3476(98)70018-6.

Wen, Y., Parikh, C.R., 2021. Crit. Rev. Clin. Lab Sci. 58, 354–368. https://doi.org/10.1080/10408363.2021.1879000.

Xie, P., Cao, X., Lin, Z., Javanmard, M., 2017. Lab Chip 17, 1939–1947. https://doi.org/10.1039/C7LC00035A.

Yeh, E.-C., Fu, C.-C., Hu, L., Thakur, R., Feng, J., Lee, L.P., 2017. Sci. Adv. 3, e1501645 https://doi.org/10.1126/sciadv.1501645.

Zeitoun, A.A.H., Gad, S.S., Attia, F.M., Maziad, A.S.A., Bell, E.F., 2010. Scand. J. Infect. Dis. 42, 299–305. https://doi.org/10.3109/00365540903449832.

Zhang, S., Li, Z., Wei, Q., 2020. Nanotechnol. Precis. Eng. 3, 32–42. https://doi.org/10.1016/j.npe.2019.12.004.